A Multi-Scale Electrochemical and Thermal Model of a $LiFePO_4$ Battery

C. Hellwig*[,a] , S. Sörgel[a] and W. G. Bessler[a,b]

[a] German Aerospace Center (DLR), Institute of Technical Thermodynamics
Pfaffenwaldring 38-40, 70569 Stuttgart, Germany
[b] Universität Stuttgart, Institute of Thermodynamics and Thermal Engineering (ITW)
Pfaffenwaldring 6, 70550 Stuttgart, Germany
* Corresponding author, Email: christian.hellwig@dlr.de

Modeling and simulation of lithium batteries is becoming of increasing importance both for improving the fundamental understanding of electrochemical processes and for developing battery management systems for practical applications. We present a 1D+1D+1D multi-scale electrochemical and thermal model of a lithium-ion battery with lithium iron phosphate ($LiFePO_4$, LFP) positive electrode material. The model uses a hierarchical representation of spatial scales: On the nanoscopic level, diffusive transport takes place in the active material particles. On the microscopic level, multi-component mass and charge transport as well as heat production is described in a single repeat unit (anode, separator, cathode, current collectors). On the macroscopic scale, the model describes heat transport in the radial direction of a cylindrical cell. Molar enthalpies and entropies are incorporated as function of state of charge (SOC) for reliable simulation of heat production. The model is validated using experimentally-determined discharge curves over a wide range of discharge currents.

Introduction

Lithium-ion batteries provide the highest energy density of all commercially relevant rechargeable battery types (1). Materials design plays a key role in development of improved lithium-ion batteries. The requirements for a good electrode material are high volumetric and gravimetric capacity to allow small but powerful battery devices, high cycling stability, high rate capability allowing for fast charge and discharge, low toxicity and low cost (2). A promising choice especially for applications in the field of electromobility is lithium-ion batteries based on lithium iron phosphate ($LiFePO_4$, LFP) positive electrodes, being able to supply high power density at significantly higher lifetime, reduced material costs and material toxicity, as well as improved operational safety (2, 3). LFP exhibits a moderate theoretical gravimetric energy density of 170 mAh/g and a flat discharge voltage of about 3.4 V vs. lithium (3).

Modeling and simulation of lithium batteries is becoming of increasing importance both for improving the fundamental understanding of electrochemical processes as well as for developing battery management systems for practical applications. Kinetic models based on a multi-scale description of chemistry and transport have been proven to be particularly useful. In the context of lithium-ion batteries, these kinds of models have been pioneered by Newman and co-workers (4, 5). Independently, we have developed previously multi-scale models based on similar approaches in the context of solid oxide fuel cells (6-8). The main philosophy of kinetic models can be summarized as follows: (1) Thermodynamic properties of the involved materials and species are used as basis for kinetic models. They determine the general shape of the battery discharge curve. (2) Chemical reaction kinetics of electron transfer, heterogeneous and/or homogeneous chemistry are integrated. This can be done either in the form of (semi)empirical Butler-Volmer type equations, or in the form of elementary reaction kinetics (8). The latter allows a parameterization on the basis of atomistic simulations. (3) Chemistry is coupled to mass, charge and heat transport. Transport processes take place on multiple scales (atoms and electrons inside the solid active materials, ions in the liquid electrolytes, electrons in the current collectors, heat within the full cells). Only kinetic models allow the prediction of macroscopic electrochemical behavior of a battery under realistic operating conditions.

Concerning batteries with LFP electrodes, only a handful of kinetic modeling studies have been published so far. The studies mostly apply the shrinking core model which was developed by Srinivasan and Newman (5, 9). In this model, it is assumed that a phase boundary between $LiFePO_4$ and $FePO_4$ moves into a spherical particle, while Li^+ diffuses from the particle surface perpendicular to the phase boundary. The model was further developed and used by several authors (10-13). Recently, a different picture has emerged that was termed domino-cascade model by Delmas et al. (14). In this model, it is assumed that Li^+ and e^- move along the phase boundary, where they have particularly high mobilities due to the strain resulting from the LFP/FP lattice mismatch. The phase front itself moves perpendicular to that direction. This situation was investigated quantitatively by Singh, Ceder and Bazant using a phase-field model (15, 16). More recently, it was argued that phase fronts within single particles are not present because of their small size, inducing rapid redistribution of lithium between individual particles (17).

In this paper we present a 1D+1D+1D multi-scale kinetic model of a cylindrical lithium-ion battery with LFP positive electrode. The model combines previous approaches from the battery and the fuel cell literature. It allows to simulate (dis-)charge curves and electrochemical impedance spectra. It is based on a physicochemical description of thermodynamics, kinetics and transport processes based on a continuum approach. Experimental investigations were carried out for parameter estimation and model validation.

Experiments

Experiments were carried out using commercial high-power cells by A123, type ANR26650M1, with a nominal capacity of 2.3 Ah, a nominal voltage of 3.3 V, and a nominal specific energy of 108 Wh/kg. These cells use LFP as positive electrode and a carbon or graphite material as negative electrode. The cells were characterized electrochemically using a Zahner IM6 frequency response analyzer. Constant-current discharge curves were recorded at currents between 50 mA and 23 A after constant-current constant-voltage (CCCV) charge. Not all experimental results are shown. Electrochemical impedance spectra were recorded in potentiostatic mode with 2 mV excitation amplitude in the frequency range of 1.2 mHz-100 kHz. A four-wire setup was used. All measurements were performed at room temperature.

For the determination of macrostructural parameters, X-ray computer tomography (CT) was performed using a Phoenix v-tome-x L450 with a nominal voxel size of 5 µm. The practical resolution in the current experiments was around 8 µm. Scanning electron microscopy (SEM) was carried out with a Zeiss ULTRA plus.

Modeling and Simulation

Multi-scale modeling domain

The multi-scale approach applied here is shown in Figure 1. The largest scale (macroscale: centimeters) represents the radial direction of a cylindrical or flat cell. This is the relevant scale for conductive heat transport and heat dissipation to the environment. In the radial direction, the cell consists of consecutive layers of single repeat units. The intermediate scale (microscale: ~ 150 µm) of the model describes mass, charge and heat transport within the repeat unit, in particular within the liquid electrolyte that immerses the pore space of electrodes and separator. The smallest scale (nanoscale: 50-1000 nm) represents the active materials particles. The model describes lithium (de-)intercalation at the particle surface and diffusion inside the particle. The three scales are coupled via respective boundary conditions. All model equations are summarized in Table I and are described and derived in the following. The model parameters are summarized in Table II.

Model description

Thermodynamics. The thermodynamic properties of the cell are modeled based on reaction enthalpies ΔH and entropies ΔS of the two half-cell reactions, that can be formulated in discharge direction as

$$\mathrm{LiC_6} \rightleftharpoons \mathrm{C_6} + \mathrm{Li^+}\,\text{(electrolyte)} + \mathrm{e^-}\,\text{(negative electrode)} \qquad [1]$$
$$\mathrm{FePO_4} + \mathrm{Li^+}\,\text{(electrolyte)} + \mathrm{e^-}\,\text{(positive electrode)} \rightleftharpoons \mathrm{LiFePO_4}\ . \qquad [2]$$

The half-cell potentials follow from enthalpies and entropies according to the Gibbs-Helmholtz Equation (Eq. 8). The separation of enthalpy and entropy contributions is a requirement for thermal simulations, particularly for the separation of heat sources into reversible and irreversible contributions. Both ΔH and ΔS depend on the Li content. We use here empirical values from literature (18-21). The thermodynamic data are plotted as a function of Li content in Figure 2. Note for both, the positive and the negative electrode, the entropy changes sign with varying Li content. This means that the irreversible heat production rate changes sign as a function of SOC. It is important to note that not the full stoichiometry range is used in the commercial cell. The actual stoichiometry range is obtained via comparison of simulated discharge curves with experimental data. The resulting values are given in Table II.

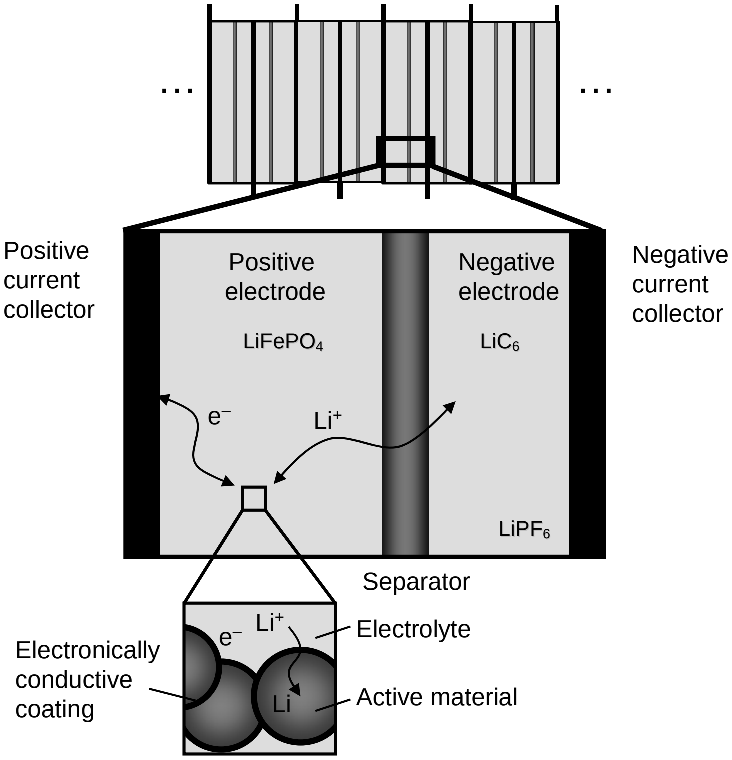

Figure 1. Multi-scale kinetic modeling of a lithium battery. On the nanoscopic scale (50-1000 nm), the model describes the active materials as spherical particles. On the microscopic scale (100-200 µm), the model describes a single repeat unit (electrodes, separator, current collectors). On the macroscopic scale (1-5 cm), multiple repeat units are combined to model heat transport in the radial direction of cylindrical or flat cells.

Kinetics. The charge-transfer reaction takes place at the surface of the particles, where we assume global reactions at anode and cathode (Eqs. 1 and 2). The reactions are reversible and are described by a Butler-Volmer equation (Eq. 9) as a function of the activation overpotential (Eq. 10). Concentration overpotentials due to electrolyte transport are explicitly modeled (Eq. 12); note the concentration overpotentials due to solid-state transport are implicitly included in the half-cell thermodynamic data. Additionally the formation of an electrochemical double layer is modeled by assuming ideal capacitive behavior (Eq. 14). The cell voltage is calculated by the difference of the electric potential between cathode and anode current collector (Eq. 15).

Solid-state diffusion. On the particle scale, transport is described as ordinary Fickian diffusion in spherical particles (Eq. 16). The chemical source term represents charge transfer at the particle surface. The diffusion coefficients of both active materials are not constant, but depend on the stoichiometry, that is, the amount of intercalated lithium in the particles. The diffusion coefficients vary by two to three order of magnitudes; they are shown in Figure 3.

Electrolyte transport. Different to the common approach of using concentrated solution theory for describing electrolyte transport (4, 5, 22), we apply here the Nernst-Planck equation to describe coupled diffusion and migration (23). We develop a general multicomponent formulation that can accommodate spatially varying diffusion coefficients. As common in computational fluid dynamics approaches, we use the mass density ρ [kg/m^3] instead of concentration c [mol/m^3] as conservation variable.

The Nernst-Planck equation describes ionic transport based on diffusion and migration,

$$\frac{\partial(\varepsilon\rho_i)}{\partial t} = \nabla\left(D_i\nabla\rho_i\right) + \frac{z_i F}{RT}\nabla\left(D_i\rho_i\nabla\phi\right) + M_i\dot{s}_i^V \quad , \qquad [3]$$

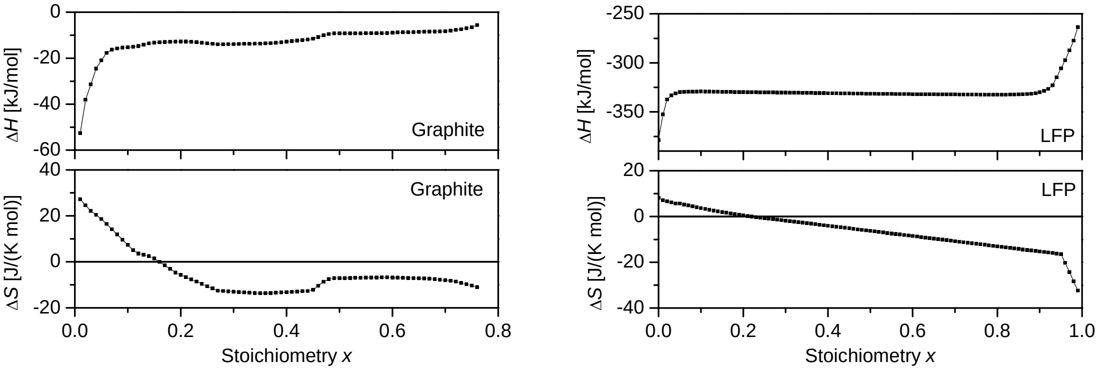

Figure 2. Thermodynamic properties (half-cell reaction enthalpies ΔH and entropies ΔS) used in the model as function of stoichiometry x of lithium in graphite (left, data from Reynier et al. and Safari et al. (18, 20)) and LiFePO$_4$ (right, data from Dodd and Safari et al. (20, 21)).

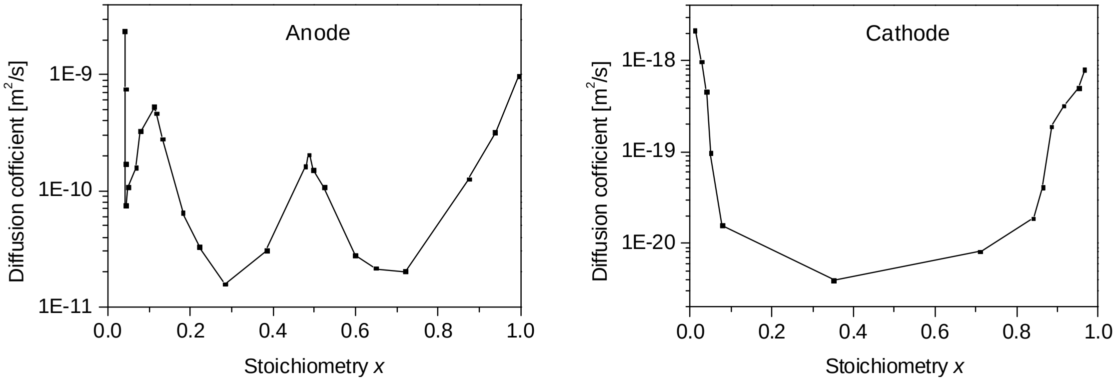

Figure 3: Diffusion coefficients for anode and cathode in dependence on the stoichiometry x (21, 24).

where ε is the porosity (depending on the location within the repeat unit), D_i [m^2/s] is the diffusion coefficient of the species i, z_i the charge of species i, F the faradaic constant, R the ideal gas constant, T [K] the temperature, ϕ [V] the electric potential, M_i [kg/mol] the molar mass and $\dot{s}_i^{\mathrm{V}}$ [mol/(m^3·s)] a chemical source term due to lithium (de-)intercalation or chemical reactions in the electrolyte (e.g., ion association, SEI formation). For n species, there are n Equations (3), but n+1 unknowns (n densities ρ_i plus the electric potential ϕ). In order to close the equation system, we assume charge neutrality,

$$\sum \left(\varepsilon c_i z_i \right) = 0 \quad . \qquad [4]$$

For developing a general multi-species formulation of the electric-potential equation, the concentration in Eq. (4) is substituted with density $\rho_i = c_i/M_i$ and the equation is derived with respect to time, yielding

$$\sum_i \frac{z_i}{M_i} \frac{\partial \left(\varepsilon \rho_i \right)}{\partial t} = \quad 0 \quad . \qquad [5]$$

This equation describes the condition for maintaining charge conservation over time. Inserting the Nernst-Planck Equation (3) into Eq. (5) yields after rearrangement

$$\nabla \sum_i \left(\frac{z_i^2 F^2}{RT} \frac{D_i \rho_i}{M_i} \right) \nabla \phi \quad = -\sum_i \left(\nabla \left(\frac{z_i D_i F}{M_i} \nabla \rho_i \right) \right) \quad - \sum_i \left(z_i F \dot{s}_i^{\mathrm{V}} \right) \quad . \qquad [6]$$

This equation has a typical form for charge conservation equations,

$$\nabla \left(\sigma \nabla \phi \right) = b \qquad [7]$$

where σ is the ionic conductivity of the electrolyte and b is a source term due to diffusion and chemical reactions of charged species. Thus, we have mathematically cast the charge neutrality condition into a form that can be easily implemented into simulation software. Note that this formulation (Eqs. 17 and 18) is applicable to multi-component mixtures of both charged and uncharged species. For uncharged species (z = 0), the Nernst-Planck Equation is reduced to an ordinary diffusion equation and the charge conservation equation is unaffected.

Heat transport. Within the cell, heat is transported via conduction (Eq. 19). The heat conductivity λ and capacity C_{P} depend on the layer (electrodes, separator, current collectors). Heat sources are due to chemistry (reversible and irreversible losses) and electrolyte resistance.

TABLE I. Model equations

Physicochemical process	Model equation	
Thermodynamics (anode and cathode)		
Half-cell equilibrium potential	$\Delta\phi_{\mathrm{eq}}(c_{\mathrm{Li}}) = -\frac{\Delta G}{zF} = \frac{\Delta H(c_{\mathrm{Li}}) - T\Delta S(c_{\mathrm{Li}})}{zF}$	[8]
Kinetics (anode and cathode)		
Butler-Volmer kinetics	$i_{\mathrm{F}}^{V} = i_0\left(\exp\left(\frac{\alpha F}{RT}\eta_{\mathrm{act}}\right) - \exp\left(-\frac{(1-\alpha)F}{RT}\eta_{\mathrm{act}}\right)\right)$	[9]
Activation overpotential	$\eta_{\mathrm{act}} = \Delta\phi - \Delta\phi_{\mathrm{eq}}(c_{\mathrm{Li}}) - \eta_{\mathrm{conc}}$	[10]
Potential step (Anode and Cathode)	$\Delta\phi = \phi_{\mathrm{electrode}} - \phi_{\mathrm{electrolyte}}$	[11]
Concentration overpotential	$\eta_{\mathrm{conc}} = \frac{RT}{zF}\ln\left(\frac{c_0}{c(t)}\right)$	[12]
Total current density	$i = \int_{y=0}^{L_{\mathrm{electrode}}}\left(i_{\mathrm{F}}^{\mathrm{V}} + i_{\mathrm{dl}}^{\mathrm{V}}\right)\mathrm{d}y$	[13]
Current density due to electrochemical double layer	$i_{\mathrm{dl}}^{\mathrm{V}}(t) = A_{\mathrm{dl}}^{\mathrm{V}}\, C_{\mathrm{dl}}(\Delta\phi)\, \frac{\partial(\Delta\phi)}{\partial t}$	[14]
Cell voltage		
Cell voltage	$E = \phi_{\mathrm{cathode}} - \phi_{\mathrm{anode}}$	[15]
Solid-state transport (anode and cathode)		
Spherical diffusion in particle	$\frac{\partial\rho_{Li}}{\partial t} = \frac{1}{r^2}\frac{\partial}{\partial r}\left(r^2 D\frac{\partial\rho_{\mathrm{Li}}}{\partial r}\right) - \frac{M_{\mathrm{Li}}}{zF}i$	[16]
Electrolyte transport		
Mass conservation	$\frac{\partial(\varepsilon\rho_i)}{\partial t} = \nabla\left(D_i\nabla\rho_i\right) + \frac{z_iF}{RT}\nabla\left(D_i\rho_i\nabla\phi\right) + M_i\dot{s}_i^V$	[17]
Charge conservation	$\nabla\left(\sigma\nabla\phi\right) = b$ with $\sigma = \sum_i\left(\frac{z_i^2F^2}{RT}\frac{D_i\rho_i}{M_i}\right)$, $b = -\sum_i\left(\nabla\left(\frac{z_iD_iF}{M_i}\nabla\rho_i\right)\right) - \sum_i z_iF\dot{s}_i^{\mathrm{V}}$	[18]
Heat transport		
Heat conduction and convection	$\frac{\partial(\rho C_{\mathrm{P}}T)}{\partial t} = \frac{\partial}{\partial y}\left(\lambda\frac{\partial T}{\partial y}\right) + \dot{Q}_{\mathrm{elchem}} + \dot{Q}_{\mathrm{ohm}} - \alpha(T_{\mathrm{cell}} - T_{\mathrm{env}})$	[19]

TABLE II. Model parameters

Parameter	Value
$LiPF_6$ concentration	1.5 mol·l^{-1}
Li^+ and PF_6^- diffusion coefficient	$1\cdot10^{-10}$ $m^2\cdot s^{-1}$
Thickness (anode / separator / cathode)	35.5 µm / 20 µm / 79.5 µm
Thickness current collector (anode / cathode)	15.0 µm / 15.0 µm
Stoichiometry range x (anode / cathode)	0.01-0.62 / 0.01-0.99
Bulk diffusion coefficients (LiC_6 / $LiFePO_4$)	Reference (21, 24) (Figure 3)
Exchange current density (anode / cathode)	$7\cdot10^6$ A·m^{-3} / $2.5\cdot10^6$ A·m^{-3}
Particle radius (anode / cathode)	3.58 µm / 0.021 µm
Total electrochemically active area	0.130 m^2

Simulations

The partial differential equations are spatially discretized using finite-volume techniques. For the repeat element simulations, we use 10 grid points for each layer (anode, separator, cathode). For full cell simulations, the number of grid points are reduced to 3 per layer for reducing computational cost, and 7 representative repeat elements are simulated along the radial dimension of the cell. The thermodynamic data (Figure 2) are implemented in the form of look-up tables; intermediate values for the Li content x are linearly interpolated. Also, the diffusion coefficients of both active materials as function of the Li content x in the particle are implemented in in form of look-up tables and linearly interpolated (see Figure 3). The model equations and simulation methodology are implemented into the in-house code DENIS originally developed for fuel cell simulations (6).

Experimental parameterization and validation

Micro- and macrostructural parameters (Table II) were experimentally determined using computer tomography and electron microscopy. The model is validated using constant-current discharge curves as well as electrochemical impedance spectra. Furthermore, temperature variation upon cycling was studied in a Netzsch ARC 254 calorimeter. All experiments were performed using commercial $LiFePO_4$-based high-power cells (A123) with 26650 geometry and a nominal capacity of 2.3 Ah. Therefore, the model directly represents the behavior of this kind of cell.

Results – Single Repeat Element

In this article, we present results for two different cases: (1) Isothermal simulations using a single repeat element only (1D+1D simulation of the two lower scales), as presented in this Section; (2) Thermal simulations using the full cell model (1D+1D+1D simulation over all scales), as presented in the next Section.

Discharge curve

Experimental and simulated discharge curves are shown in Figure 4. The curves were recorded for constant currents between 230 mA and 10.5 A, that is, they reflect a variation over one and a half orders of magnitude. There is quantitative agreement between model and experiment over this complete range concerning discharge capacity and general voltage shape. Yet, there are a few differences in the fine structure. These differences are connected to the thermodynamic data used as basis for the present simulations. Obviously, the thermodynamic properties used in the simulations differ from those in the experimental cells, although partially data from these experimental cells are used from literature (18-21). The simulation for a 4.6 C-rate shows a lower cell potential over the whole capacity range and an earlier drop to a lower voltage than the experiments. Due to the fact that these simulations are isothermal, the better performance of the experimtental cell may be explained by internal heating during discharge.

It is important to emphasize that this model use neither empirical polynomials for half-cell potentials (as typical in battery modeling literature) nor measured full-cell discharge curves (as typical in equivalent circuit models). Instead, experimental literature data of similar, yet not identical materials systems are applied. If these data were made available for the same cells used here for model validation, the remaining discrepancy between model and experiment would be largely reduced.

Electrochemical impedance

Electrochemical impedance spectroscopy allows to investigate processes occurring on different time scales which correlate with the applied frequency of current (galvanostatic mode) or voltage (potentiostatic mode). Figure 5 shows simulations and experimental results of electrochemical impedance spectroscopy for different SOC at open circuit. We chose a Bode representation, where the real and the imaginary part of the impedance are plotted versus logarithmic frequency. Three frequency ranges can be identified. The high-frequency range shows the behavior due to ohmic resistance and inductance. The intermediate-frequency range between 1 and 1000 Hz can be related to charge transfer and double layer processes. In the low-frequency range below 1 Hz diffusion and discharge processes become dominant.

The impedance simulations show an overall good agreement with the experiment. It is important to realize that these simulations are based on a physical model with one single set of parameters used for all conditions. Although equivalent circuit type models usually reproduce experimental data with better agreement that shown here, they are based on a large number of empirical parameters fitted individually for every data set.

Spatial concentration variations

Kinetic models allow the *in situ* investigation and quantification of the behavior inside the cell that is not accessible experimentally. This behavior changes with different C-rates and has a great impact on the performance of the battery. During discharge, Li^+ ions migrate from the anode to the cathode. This results in a concentration gradient in the electrolyte which is shown in Figure 6 (dashed line) at at SOC of 25 % after 1C discharge. At the anode, Li^+ ions enter the electrolyte, increasing the concentration from 1.5 mol/l (initial concentration) to 1.6 mol/l. At the cathode, Li^+ ions intercalate, decreasing the concentration. The resulting concentration gradient induces diffusion of the Li^+ ions from the anode to the cathode. The concentration gradient also induces spatially varying charge-transfer kinetics. Close to the separator the (de-)intercalation is faster than close to the current collectors. This leads to spatially varying solid-phase Li content, shown as solid lines in Figure 6. Here, the SOC of the positive electrode varies between ca. 65 % and 75 %. The gradients are much more pronounced at higher C-rates (not shown).

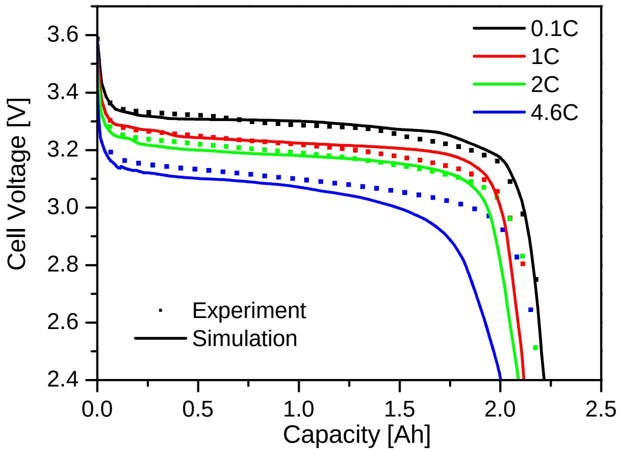

Figure 4: Simulated and experimental constant-current discharge curves.

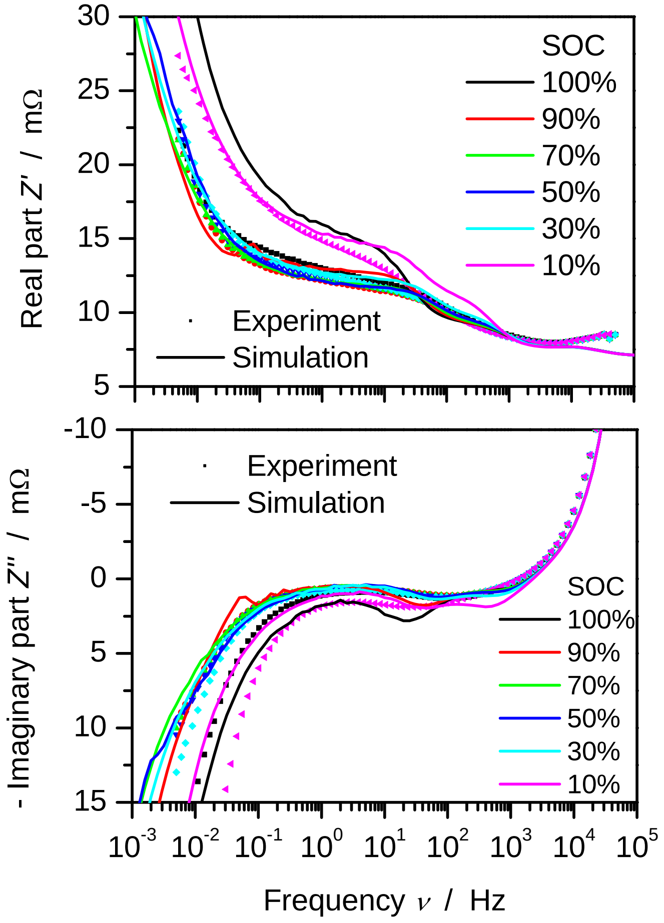

Figure 5: Comparison of experimental (dotted lines) and simulated (solid lines) electrochemical impedance spectra. Real and imaginary parts of the impedance versus frequency are shown for different state of charges (SOC).

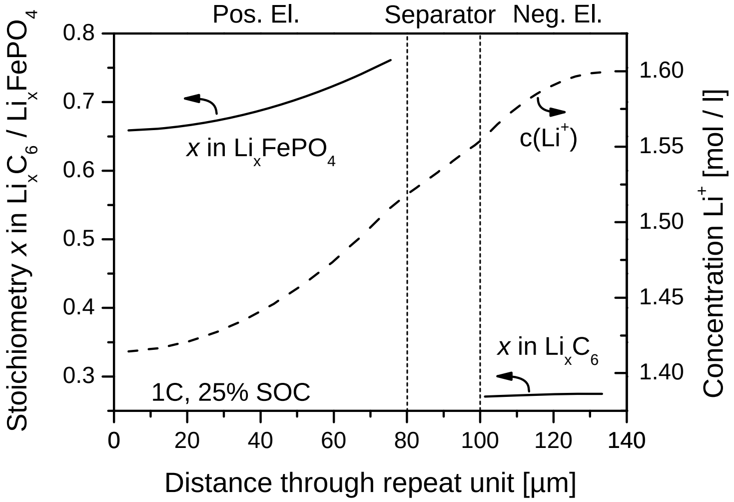

Figure 6: Spatial distributions of the concentration of Li^+ in the electrolyte (dashed line) and the intercalated Li in the electrodes (solid lines) along the length of one repeat-unit. The data are shown for a state-of-charge of 25% after discharging with 1C-rate.

Results – Full Cell

Temperature variation upon cycling

The temperature distribution in a cell strongly influences performance, ageing, side reactions, and safety. Measured and simulated cell surface temperature are shown together with the cell voltage in Figure 7. Data are shown for a repeated charge and discharge cycle at 1C rate, starting from an empty battery at a surrounding temperature of 35 °C. Upon first charging, the experiments show a continuous increase of the temperature from 35 °C to around 40 °C. In the consecutive cycles, temperature shows a non-monotonic behavior with variations between of 39 °C and 40 °C. The simulations show the same qualitative behavior, although the absolute temperature increase is considerably lower than in the experiments. The origin for this discrepancy is yet unclear.

The heat production rate within the cell, as predicted by the simulation, is shown in Figure 8 for the same cycle. The electrochemical contribution to cell heating is strongly varying. It is highest close to the fully charged and discharged cells. Under these moderate C-rates, the origin of the electrochemical heating is mostly reversible entropy losses. The curve thus reflects the thermodynamic properties of the electrode materials (Figure 2). Joule heating due to electrolyte resistance is low and is not dominantly contributing.

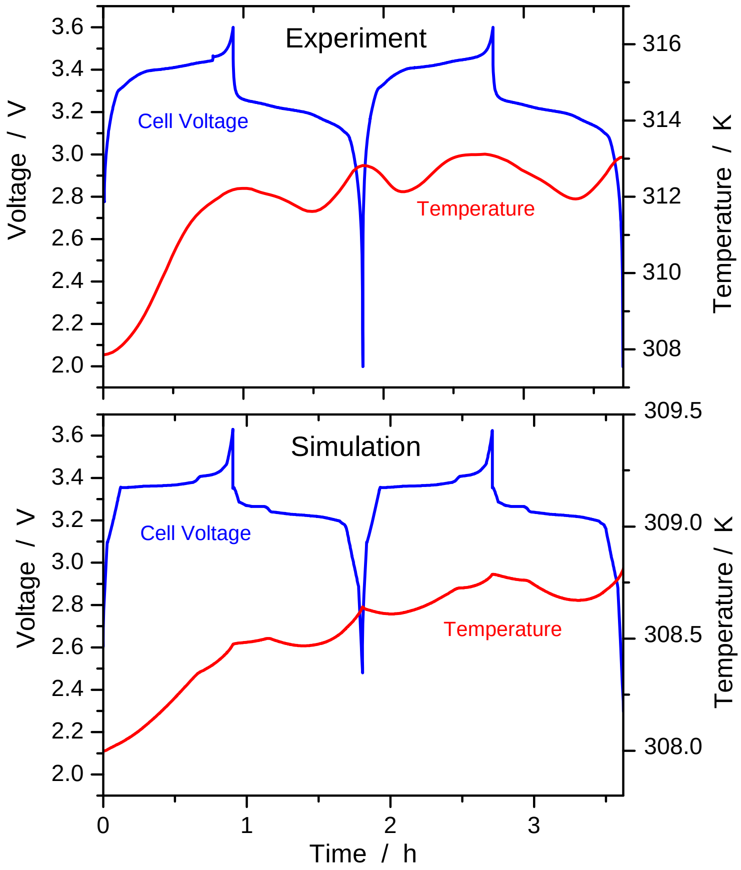

Figure 7: Experimental (upperplot) and simulated (lowerplot) cell temperature and voltage during two consecutive charge/discharge cycles of the cell.

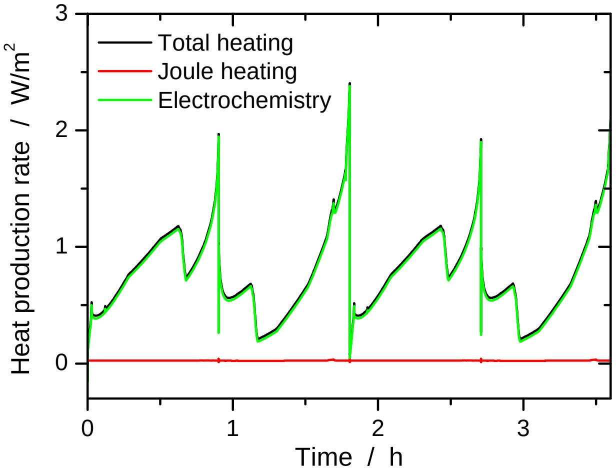

Figure 8: Simulated heat production rates due to Ohmic electrolyte resistance (Joule heating) as well as reversible and irreversible electrochemistry for the cycles shown in Figure 7.

Conclusions

We have presented a 1D+1D+1D multi-scale model for lithium-ion batteries. It represents the structure of a complete cell in the radial direction. Each repeat unit consists of multiple layers (composite electrodes, separator, current collectors). In each electrode, solid-state diffusion within the active material particles is considered. Thermodynamic half-cell properties of graphite and $LiFePO_4$ and particularly the individual contributions of enthalpy and entropy as function of intercalation stoichiometry are included. Charge-transfer kinetics is described with traditional Butler-Volmer equations. A general multi-component formulation of electrolyte transport was derived and cast into a mathematical form that can conveniently be implemented in simulation software.

Simulated discharge curves were compared with experimental data from commercial high-power cells over a wide range of current values. The model quantitatively reproduces experimental data. Remaining discrepancies are due to different half-cell thermodynamic properties of the commercial cells as compared to the literature data. Simulated concentration distributions within the repeat unit show a rather large (~ 15 %) spatial variation of the state-of-charge of the half cells even at moderate (1C) discharge rates. Thermal variations upon cycling can be explained by entropy effects of the active materials.

Acknowledgments

The authors thank Julian Daubenschmid and Wolfgang Mielke for supporting the setup of the thermal model. The authors also thank Dr. Robert Ruckdäschel, Ina Plock, Dr. Günter Schiller and Dr. Norbert Wagner (all German Aerospace Center, Stuttgart) for their support in acquisition and interpretation of SEM, CT and EIS data, respectively. WGB acknowledges funding by the Initiative and Networking Fund of the Helmholtz Association.

References

1. M. Yoshio, R. J. Brodd and A. Kozawa, *Lithium-Ion batteries: Science and technologies*, Springer, New York (2009).
2. Z. Li, D. Zhang and F. Yang, *J. Mater. Sci.*, **44**, 2435 (2009).
3. A. K. Padhi, K. S. Nanjundaswamy and J. B. Goodenough, *J. Electrochem. Soc.*, **144**, 1188 (1997).
4. J. Newman and W. Tiedemann, *AIChE J.*, **21**, 25 (1975).
5. V. Srinivasan and J. Newman, *J. Electrochem. Soc.*, **151**, A1517 (2004).
6. W. G. Bessler, S. Gewies and M. Vogler, *Electrochim. Acta*, **53**, 1782 (2007).
7. W. G. Bessler, *Solid State Ionics*, **176**, 997 (2005).
8. S. B. Adler and W. G. Bessler, in *Handbook of Fuel Cells - Fundamentals, Technology and Applications, Vol. 5*, W. Vielstich, H. Yokokawa and H. A. Gasteiger Editors, p. 441, John Wiley & Sons, Chichester, UK (2009).
9. K. Striebel, J. Shim, V. Srinivasan and J. Newman, *J. Electrochem. Soc.*, **152**, A664 (2005).
10. C. S. Wang, U. S. Kasavajjula and P. E. Arce, *Journal of Physical Chemistry C*, **111**, 16656 (2007).
11. U. S. Kasavajjula, C. S. Wang and P. E. Arce, *Journal of the Electrochemical Society*, **155**, A866 (2008).
12. S. Harinipriya, V. D. Diwakar and V. R. Subramanian, *Journal of the Electrochemical Society*, **155**, A875 (2008).
13. M. A. Roscher, J. Vetter and D. U. Sauer, *J. Power Sources*, **191**, 582 (2009).
14. C. Delmas, M. Maccario, L. Croguennec, F. Le Cras and F. Weill, *Nature Materials*, **7**, 665 (2008).
15. B. C. Han, A. van der Ven, D. Morgan and G. Ceder, *Electrochim. Acta*, 4691 (2004).
16. G. K. Singh, G. Ceder and M. Z. Bazant, *Electrochimica Acta*, **53**, 7599 (2008).
17. W. Dreyer, J. Jamnik, C. Guhlke, R. Huth, J. Moskon and M. Gabarscek, *Nature Materials*, **9** (2010).
18. M. Safari and C. Delacourt, *Journal of The Electrochemical Society*, **158**, A562 (2011).
19. Y. Reynier, R. Yazami and B. Fultz, *Journal of Power Sources*, **119-121**, 850 (2003).
20. J. L. Dodd, PhD thesis, in *California Institute of Technology* (2007).
21. M. Safari and C. Delacourt, *Journal of The Electrochemical Society*, **158**, A63 (2011).
22. K. A. Smith, C. D. Rahn and C.-Y. Wang, *Energy Conversion and Management*, **48**, 2565 (2007).
23. D. Danilov and P. H. L. Notten, *Electrochim. Acta*, **53**, 5569 (2008).
24. M. D. Levi and D. Aurbach, *The Journal of Physical Chemistry B*, **101**, 4641 (1997).